Supporting Information

Alford et al. 10.1073/pnas.1105860108

SI Text

Online Methods. ***Muscular thin films and microcontact printing.*** Vascular muscular thin films (1) were constructed by spin-coating poly(N-isopropylacrylamide) (PIPAAm) (Polysciences, Warrington, PA) onto a prestretched elastomer membrane (SMI .010" NRV) then spin-coating polydimethylsiloxane (PDMS) (Sylgard 184, Dow Corning, Midland, MI) doped with 0.2 μm diameter fluorospheres (Invitrogen, Carlsbad, CA) on the PIPAAm. The construct was then cured at 65 °C for 4 h. Fibronectin (BD Biosciences, Sparks, MD) was microcontact printed (2) onto the PDMS layer, as previously published (3), in 10 μm wide lines separated by 10 μm wide gaps to provide alignment cues for seeded cells. For imaging and biochemistry experiments tissues were patterned directly onto the PDMS membrane, using the same technique.

Cell culture. Human umbilical artery vascular smooth muscle cells (VSMCs) were purchased from Lonza at passage 3 and cultured in growth medium consisting of M199 culture medium (GIBCO, Invitrogen, Carlsbad, CA) supplemented with 10% fetal bovine serum (Invitrogen), 10 mM Hepes (GIBCO, Invitrogen, Carlsbad, CA), 3.5 g/L glucose, 2 mg/L vitamin B-12, 50 U/mL penicillin and 50 U/mL streptomycin (GIBCO). All experiments were performed at passage 5–7. VSMCs were seeded at 25,000 cells/cm², creating a confluent tissue, and incubated in growth medium for 24 h. Growth medium was then replaced with serum free medium, to induce a contractile phenotype (4), for 24 h prior to simulated blast.

Simulated blast by high-velocity stretching. We assume that the main mechanical loading during blast is the pressure wave is traveling through the lumen (5, 6). To simulate a blast pulse traveling through the vasculature we applied a high-velocity acute uniaxial stretch in the direction of tissue alignment (Movie S1), similar to methods used to simulate astrocyte and neuronal injury in vitro (7, 8). This deformation mimics luminal expansion due to dynamically increasing pressure. Tissues were built on 5 × 8 cm elastomer substrates, with a thickness of 0.01". A linear motor (Linmot, PS01-23x80F) was used to displace one end of the substrate 2.5 mm for 5% strain and 5 mm for 10% strain at a rate of 500 mm/s. The deformation was measured by marking the substrate with an ink dot array and recording the deformation at 1,000 frames/s using a FasTec Troubleshooter Model #: TS1000ME camera (Movie S2). The strain field of the substrate was measured using a three-point strain algorithm (9). The mean strain field can be found in the main body Fig. 1B.

Quantification of cytoskeletal and nuclear alignment. Tissues exposed to simulated blast were stained for F-actin (phalloidin) and nuclei (DAPI). Actin orientation was calculated from phalloidin staining as in Bray et al. (10). Nuclear orientation was calculated by fitting an ellipse to each individual nucleus and calculating the orientation of the major axis of the ellipse (11). Both orientations were quantified for ten images in a single tissue and the total orientational order parameter (12) was calculated for each tissue (Fig. S1 A–C).

Membrane poration. To test whether the membrane was porated during simulated blast (13), we added fluorescein dye (Invitrogen, Carlsbad, CA) to the media at a concentration of 10 μM 15 min prior to the blast. After blast, five minutes, the tissues were fixed and stained with DAPI. Tissues with fluorescent intensity three standard deviations above the image mean were considered to be porated (Fig. S1 A–C).

Cytosolic calcium measurement. Fluo-4 AM calcium indicating dye (Invitrogen) was suspended in Pluoronic F-127 at .5 μg/μL. After simulated blast, thirty minutes, the dye was added to the tissues at a dilution of 1:200 for 15 min. The dye was washed out and allowed to equilibrate for 15 min. Fluorescent intensity was measured 1 frame/s for 30 min using line scanning confocal microscopy (Zeiss 5 Live, Carl Zeiss, Oberkochen, GER). The untreated tissue was imaged for 10 min to acquire spontaneous transients, then ET-1 (Sigma-Aldrich, St Louis, MO) was added to the far end of the well and allowed to diffuse to the observed region. To quantify the temporal transients, transients for numerous regions of interest were measured and normalized by the fluorescent intensity prior to transient onset, giving the change in fluorescent intensity, F/Fo. Individual traces were then registered with other transients by onset time (Fig. 1 G and I). Additionally, each cell's maximum F/Fo was also measured, regardless of the peak time, and quantified (Fig. 1H). Peaks were compared using Kruskal-Wallis ANOVA on ranks with pairwise comparisons using Dunn's method.

vMTF stress measurement. Vascular muscular thin film tissue stresses were calculated as previously published (3). Briefly, prior to the experiment, the tissues are cultured at 37 °C. At the time of the experiment, the tissue and PDMS layers of the construct are cut into strips and the medium is allowed to cool below 32 °C, melting the PIPAAm layer. The free-floating vMTFs were then transferred to a separate dish where they were attached to PTFE coated posts such that their radius of curvature could be observed (3). The vMTFs were maintained at 37 °C in a bath of Tyrode's solution. The vMTFs were stimulated serially with 50 nM ET-1 followed by 100 mM HA-1077 (Sigma-Aldrich, St Louis, MO) (Fig. S2). The radius of curvature was measured under a stereomicroscope (Ziess Lumar V12, Carl Zeiss, Oberkochen, GER) in both brightfield and fluorescence. The tissue stress was calculated by assuming that the vMTF is a two-layer beam with one passive layer (PDMS) and one active layer (VSMCs) (see ref. 3 for details). The serial stimulation allows measurement of the basal contractile tone, or contraction stress prior to any stimulation, and the ET-1 induced contraction (Fig. S2), which are reported. All vMTF experiments are normalized by the control sample on the day of the experiment to account for cell variability across experiments. Stress data was compared using one-way analysis of variance (ANOVA) with pairwise comparisons done using a Tukey test.

PDMS layer and tissue layer thickness are needed to calculate vMTF stress (1, 3). Thicknesses were measured using stylus profilometry (Dektak 6M, Veeco Instruments, Inc., Plainview, NY) and confocal microscopy (Fig. S4), respectively.

Stress relaxed vMTFs. To test the effect of tension at the time of the blast, tissues were treated with 100 μM HA-1077 for 30 min prior to simulated blast. Immediately after the blast, the HA-1077 was washed out and vMTF contractility was measured as described.

To test the effect of postblast hypercontraction on contractility, tissues were treated with 10 μM HA-1077 immediately following simulated blast. HA-1077 was washed out 30 min prior to vMTF experiments, which were performed as before.

Western blotting. RIPA buffer contained 50 mM Tris, pH 8.0, 150 mM NaCl, 0.1% SDS, 1.0% NP-40, 0.5% sodium deoxycholate and protease inhibitor cocktail (Complete mini, Roche). Criterion 4%–15% polyacrylamide gels (Bio-Rad, Hercules, CA) were loaded with 20 mg of total protein and the gel was run for 1.5 h at 150 V. The gel was transferred to PVDF membranes for Western analysis. Primary antibodies used were Smooth-muscle myosin heavy chain (1:10, Leica, Bannockburn, IL), smoothelin (1:100, Milipore, Billerica, MA) and beta actin (1:5,000, Santa Cruz Biotechnology, Santa Cruz, CA). Secondary antibodies were conjugated with infrared labels (1:15,000, Licor, Lincoln, NE) and imaged with a Licor Odyssey reader (Licor, Lincoln, NE). Quantification was performed by densitometry analysis using Odyssey 3.0. Statistical comparisons were done using Mann-Whitney rank sum tests.

RT-PCR. Total RNA was collected using a Stratagene Kit (Agilent Technologies, Santa Clara, CA) according to the manufacturer's specifications. Total RNA was reverse transcribed into cDNA using an iScript cDNA synthesis kit (Bio-Rad, Hercules, CA) according to the manufacturer's specifications. Primers were purchased from RealTimePrimers.com. Forward and reverse primers were: MYH11: 5′-AGCCAGAGACGAGAGGACAT-3′ and 5′-ACGGTTTCCTGGAACATCTC-3′, SMTN: 5′-TGTGACCACAGTGACACTCC-3′ and 5′-AGAAGCTTGTT-GACCACCTG-3′, and ACTB: 5′-GGACTTCGAGCAAGA-GATGG-3′ and 5′- AGCACTGTGTTGGCGTACAG -3′. Ssofast Evagreen supermix was used for the reaction. After an initial denaturation, 52 cycles were performed with the parameters 95 °C for 5 s, 58 °C for 5 s, 72 °C for 30 s. MYH11 and SMTN expression were normalized by ACTB expression. Statistical comparisons were done using Mann-Whitney rank sum tests.

Model formulation. Arteries have a robust ability to remodel in response to internally and externally applied stresses. The surprising 24 h contractility experiments (Fig. 2) led us to hypothesize that severely injured tissues (10% strain) were undergoing a large-scale remodeling of their stress state in response to blast-induced hypercontractiility. This remodeling is difficult to directly measure, so we developed a mathematical model based on previously published tissue growth and remodeling models (14–21). First, we found that the standard assumptions of stress-induced growth and remodeling were not able to capture our experimental results. However, when we added dynamic phenotype switching, capturing the complex physiological behavior of VSMC in transforming between their two roles of providing contractile tone and actively remodeling their environment, the model captured the observed contractility behavior. Moreover, the model predicted that large strain tissues would have a decreased fraction of contractile cells, which was later experimentally validated.

The primary assumptions of the model are that mechanical stress is the transducer of long-term remodeling and phenotypic behavior, and that tissue phenotype shifts to optimize this remodeling. VSMCs assume one of two phenotypes: contractile and synthetic (22, 23). Cells with a contractile phenotype contract, but do not migrate, proliferate or significantly turn over the extracellular matrix. Conversely, synthetic cells migrate, proliferate and remodel the ECM, but generate very little contractile stress. Thus, each phenotype plays an important role in maintenance of optimal tissue tension.

The following is the formulation of this theory for a highly aligned tissue patterned in a constrained geometry on a 2D surface. All parameters of the model are listed in Table S1.

Constitutive equations. Our engineered vascular tissue is constrained to the micropatterned area on which it is seeded. Thus,

at all times, other than during simulated blast, the total tissue size and shape does not change. As a result, we consider an incompressible 1D fixed block of tissue that does not change length. Under this assumption there is no external load, only internally generated stress.

Stress is a function of the elastic deformation, i.e., the deformation from the zero-stress configuration to the current configuration. In a traditional engineering material the elastic deformation is the observable deformation from an unloaded to loaded configuration. In active biological materials, however, elastic deformation is not necessarily identical to the observed deformation. In vascular tissue, stress can be generated by contraction and remodeling, independent of changes in continuum level deformation. For example, if a tissue contracts but is constrained such that it cannot displace, it will still generate a stress, but this change in stress will not correspond with a change in strain. However, if the tissue is completely unconstrained, contraction will cause a measurable change in strain, via muscle shortening, but because it is not acting against a constraint, it will not generate stress. This stress-free shortening redefines the zero-stress configuration. Thus, tissue stress is an interplay between stresses due to elastic deformation and internally generated stresses.

In general form, total deformation ($\mathbf{F}$) can be decomposed (Fig. S5A) into elastic deformation ($\mathbf{F_e}$), growth, and remodeling deformation ($\mathbf{F_g}$), which is the change in length of the zero-stress configuration due to growth and remodeling, and active deformation ($\mathbf{F_a}$), which is the change in length of the zero-stress configuration due to contraction. Total deformation is defined as

$$\mathbf{F} = \mathbf{F_g} \cdot \mathbf{F_a} \cdot \mathbf{F_e}. \qquad [\text{S1}]$$

By definition, stress is a function of elastic deformation

$$\boldsymbol{\sigma} = \mathbf{F_e} \cdot \frac{\partial W(\mathbf{F_e})}{\mathbf{F_e^T}} - p\mathbf{I}, \qquad [\text{S2}]$$

where σ is Cauchy stress, W is the strain-energy density function of the material, p is a Lagrange multiplier and $\mathbf{I}$ is the identity matrix.

Elastic material properties are defined by their strain-energy density function (W). A number of strain-energy density functions have been used to model vascular tissue (16–18, 24, 25). Here, for simplicity, we assume that the tissue is Neo Hookean with the form

$$W = C(I_{e1} - 3), \qquad [\text{S3}]$$

where C is a material constant and I_{e1} is the first strain invariant of the elastic deformation tensor. We assume that the tissue is shear free, such that

$$\mathbf{F_e} = \text{diag}(\lambda_{e1}, \lambda_{e2}, \lambda_{e3}) \qquad [\text{S4}]$$

and

$$I_{e1} = \lambda_{e1}^2 + \lambda_{e2}^2 + \lambda_{e3}^2, \qquad [\text{S5}]$$

where λ is the stretch ratio in the subscripted direction, with the 1 direction being the axis of tissue alignment, and λ_e is the elastic stretch ratio. We also assume that the tissue is fixed at both ends (i.e., tissue length does not change), defined as

$$\lambda_1 = 1. \qquad [\text{S6}]$$

We assume that the tissue is elastically incompressible, thus

$$\lambda_{e1}\lambda_{e2}\lambda_{e3} = 1. \qquad [\text{S7}]$$

We also assume the tissue is unconstrained and stress-free perpendicular to the primary axis of alignment, which with [Eq S7] gives

$$\lambda_{e2} = \lambda_{e3} = \frac{1}{\sqrt{\lambda_{e1}}}. \qquad \textbf{[S8]}$$

Eqs **S2**, **S3**, and **S8** can be used to solve for the Lagrange multiplier p

$$p = 2C\lambda_{e2}^2 = 2C\lambda_{e1}^{-1}. \qquad \textbf{[S9]}$$

Thus, Eqs. **S2**, **S3** and **S9** give the Cauchy stress in the direction of cell alignment as

$$\sigma_1 = 2C(\lambda_{e1}^2 - \lambda_{e1}^{-1}). \qquad \textbf{[S10]}$$

We let contraction and remodeling act to modulate the stress along the primary axis of alignment only. Thus the active tensor Eq. **S1** is defined as

$$F_a = \mathrm{diag}(\lambda_a, 1, 1), \qquad \textbf{[S11]}$$

where λ_a is the stretch ratio describing the 1D change in stress-free length due to contraction (Fig. S5A) (i.e., λ_a is the ratio of the contracted length over passive length of the tissue if it is fully unconstrained.). Similarly, the remodeling tensor (Eq. **S1**) is defined as

$$F_g = \mathrm{diag}(\lambda_g, 1, 1). \qquad \textbf{[S12]}$$

Thus, for a contracting and remodeled tissue, total deformation in the direction of tissue alignment can be written as

$$\lambda_1 = \lambda_g \lambda_a \lambda_{e1}. \qquad \textbf{[S13]}$$

Combining Eqs. **S6**, **S10**–**S13** stress can be defined by the active and remodeling stretch ratios, such that

$$\sigma = 2C((\lambda_a \lambda_g)^{-2} - \lambda_a \lambda_g). \qquad \textbf{[S14]}$$

Phenotype mixture. The tissue is composed of a mixed population of contractile and synthetic cells whose zero-stress configurations differ. The stress of the tissue is dependent on the fraction of the population of each cell type. The total stress of the constrained mixture (26) is defined as

$$\sigma = \phi_c \sigma_c + \phi_s \sigma_s, \qquad \textbf{[S15]}$$

where subscripts c and s indicate contractile or synthetic phenotype, σ is Cauchy stress and ϕ is the fraction of cells in the tissue that exhibit the subscripted phenotype. Because all cells are either contractile or synthetic, phenotype fraction follows the relationship

$$\phi_c + \phi_s = 1. \qquad \textbf{[S16]}$$

Stress in contractile cells is described by Eq **S14**. However, in synthetic cells we assume no tension due to contraction ($\lambda_a = 1$). Thus, combining Eqs. **S14** and **S16**, the total tissue stress is described by

$$\sigma = 2C[\phi_c((\lambda_a \lambda_g)^{-2} - \lambda_a \lambda_g) + \phi_s(\lambda_g^{-2} - \lambda_g)]. \qquad \textbf{[S17]}$$

To calculate induced contraction and basal tone, we simulated contraction and relaxation of the tissue by dictating a change in contraction stretch ratio λ_a and recalculate Eq **S17**. Endothelin induces increased shortening of the cells. Thus for ET-1 stimulation, we let $\lambda_a = 0.6$ (17) and σ is recalculated. The difference between the stimulated stress ($\lambda_a = 0.6$) and baseline stress is the equivalent of the ET-1 induced contraction found experimentally. Basal tone is calculated similarly, with $\lambda_a = 1$, representing full relaxation.

Remodeling and phenotype switching. We assume that the tissue has a target stress (σ_o) that it strives to maintain. This assumption has been previously used to capture tissue growth and remodeling dynamics in a number of systems (15). Perturbation from the target stress-induces tissue-level remodeling. We assume that there is a linear relationship between the magnitude of the perturbation from the target stress and the rate of change of λ_g. Additionally, we assume that the rate of change of λ_g is proportional to the fraction of cells that are synthetic so that

$$\frac{\dot{\lambda}_g}{\lambda_g} = \frac{\phi_s}{\tau_\sigma}(\sigma - \sigma_o) + \frac{\phi_s}{\tau_a}(\lambda_a - \lambda_{ao}), \qquad \textbf{[S18]}$$

where $\dot{\lambda}_g$ is the time derivative of λ_g and τ_σ and τ_a are time constants. The second term is necessary to bring the tissue back to tone equilibrium (17).

Here, we present three conditions for phenotype switching: constant phenotype, linear phenotype switching, and nonlinear phenotype switching. In each, it is assumed that at equilibrium, 80% of the cells are contractile and that remodeling is not complete until this equilibrium is returned. Thus the target distribution of contractile and phenotype cells are defined as $\phi_{co} = 0.8, \phi_{so} = 0.2$.

In the constant phenotype model we assume that there is no change in phenotype fractions so that

$$\phi_c = \phi_{co}, \qquad \phi_s = \phi_{so} \qquad \textbf{[S19]}$$

at all times. This assumption is consistent with previous models (16, 17, 27, 28).

The second model assumes that perturbation from the target stress induces a shift toward the synthetic phenotype to facilitate more rapid remodeling. We assume a linear relationship between the rate of change of the phenotype and the absolute value of the magnitude of perturbation such that

$$\dot{\phi}_c = -\frac{1}{T_{\phi\sigma}}|\sigma - \sigma_o| + \frac{1}{T_{\phi\phi}}(\phi_{co} - \phi_c), \qquad \textbf{[S20]}$$

where $\dot{\phi}_c$ is the time derivative of ϕ_c, and $T_{\sigma\phi}$ and $T_{\phi\phi}$ are time constants. The first term represents and stress-induced phenotype switch, while the second term acts to return the phenotype distribution back to equilibrium.

The third model, presented in the main body of the paper, assumes that small perturbations from the target stress will induce a shift toward a contractile phenotype, as contraction is a quicker and more energetically favorable way to regulate tension. For perturbations greater than 20% of the target stress, the cells shift toward a synthetic phenotype, which is necessary for tissues to undergo large-scale remodeling (22, 23). This relationship is given by

$$\dot{\phi}_c = -\frac{1}{\tau_{\phi\sigma}}\left(\frac{-1}{(\gamma\sigma_o)^2}|\sigma - \sigma_o|^2 + \frac{2}{\gamma\sigma_o}|\sigma - \sigma_o|\right) + \frac{1}{\tau_{\phi\phi}}(\phi_{co} - \phi_c),$$

$$\textbf{[S21]}$$

where γ is a constant defined such that 2γ represents the value of $\frac{|\sigma - \sigma_o|}{\sigma_o}$ where the phenotype transitions toward synthetic cells. $\tau_{\phi\sigma}$ and $\tau_{\phi\phi}$ are time constants, as in Eq **S20** (see Fig. S8A).

Protocol. At equilibrium, $\lambda_a = 0.9$, $\sigma = \sigma_o$, $\phi_c = \phi_{co}$, and $\phi_s = \phi_{os}$. The model starts with $\sigma = 0$ and is allowed to equilibrate. We assume that blast exposure induces the tissue to acutely hypercontract, consistent with experimental results. At time $t = 0$, we proscribe an acute hypercontraction followed by a temporal return to equilibrium, described by

$$\lambda_a = 0.9 - \alpha e^{-\beta t}, \qquad \text{[S22]}$$

where α is a constant that is dependent on the degree of hypercontraction, assumed to be proportional to the blast severity (Fig. 3A), and β is a time constant and t is time after blast injury. This contraction leads to increased tissue tension Eq. **S16**. Temporal evolution of tissue tension induces remodeling and phenotype evolution, which is calculated using the finite difference method and the rate of change of remodeling Eq. **S18** and phenotype switching Eqs. **S18–S20**.

Induced contraction is calculated by setting $\lambda_a = 0.6$ and calculating the change in stress from the unstimulated tissue. Similarly, basal tone is calculated by setting $\lambda_a = 1$ and comparing the resulting stress to the unstimulated tissue (Fig. S6).

Model results. Acute hypercontraction induces elevated tissue tension in all models (Fig. S7 *A* and *F*). Temporal restoration of the target stress and changes in induced contraction and basal tone are determined by both the severity of the hypercontraction and the phenotype switching assumptions.

In the constant phenotype model, elevated tension does not affect the phenotype distribution in the tissue, leading to an immediate decrease in ET-1 induced contraction and increase in basal tone for all injured tissues. More severely injured tissues show a greater decrease in induced contraction (Fig. S7 *B* and *D*) and a greater increase in basal tone (Fig. S7 *C* and *E*). This trend is inconsistent with experimentally measured induced contraction and basal tone where moderately injured tissues increase both induced contraction and basal tone while severely injured tissues

see slight decreases in both. Thus, the assumption of basic stress-induced remodeling does not describe the postblast tissue.

In the linear phenotype switching model, elevated tension caused by blast-like injury induces a shift in phenotype toward a more synthetic population (Fig. S7*I*). Here, the more severe the injury, the greater the increase in synthetic phenotype, leading to marked decreases in induced contraction for all injured tissues (Fig. S7 *G* and *J*) with more severely injured tissue showing greater decreases. This result is still inconstant with experimental induced contraction results. However, basal tone response in this model is dependent on the severity of the injury. Mildly injured tissues show increased basal tone, while severely injured tissues have decreased basal tone (Fig. S7 *H* and *K*). This trend is consistent with experimental data.

In the nonlinear phenotype switching model, mildly injured tissues increase their contractile phenotype population fraction, while severely injured tissues increase their synthetic phenotype population fraction (main text) consistent with Eq. **S20**. Under these assumptions, mildly injured tissues display an increased induced contraction (Fig. 3 *C* and *F*) and basal tone (Fig. 3 *D* and *G*), while severely injured tissues had decreases in both. These trends are consistent with experimentally observed results and suggests that this type of dynamic phenotype switching may be responsible for the dichotomic contractile dynamics of the blasted tissue 24 h after injury.

In the main text, we have chosen $\gamma = 0.1$, which sets the transition to synthetic phenotype switching at a 20% perturbation from the target stress. To demonstrate that the value of γ does not have a qualitative effect on the behavior of the tissue we ran a parameter study wherein we varied γ and calculated induced contraction, basal tone and tissue phenotype. Fig. S8 shows the temporal change in each output with increasing blast injury. The results show that qualitatively, the value of γ does not change the result. However, it does change the degree of blast injury and resulting hypercontracton that is necessary to induce a phenotypic switch (Fig. S8*C*).

1. Feinberg AW, et al. (2007) Muscular thin films for building actuators and powering devices. *Science* 317:1366–1370.
2. Chen CS, Mrksich M, Huang S, Whitesides GM, Ingber DE (1997) Geometric control of cell life and death. *Science* 276:1425–1428.
3. Alford PW, Feinberg AW, Sheehy SP, Parker KK (2010) Biohybrid thin films for measuring contractility in engineered cardiovascular muscle. *Biomaterials* 31:3613–3621.
4. Han M, Wen J-K, Zheng B, Cheng Y, Zhang C (2006) Serum deprivation results in redifferentiation of human umbilical vascular smooth-muscle cells. *Am J Physiol Cell Physiol* 291:C50–58.
5. Cernak I, Wang Z, Jiang J, Bian X, Savic J (2001) Ultrastructural and functional characteristics of blast injury-induced neurotrauma. *J Trauma* 50:695–706.
6. Courtney AC, Courtney MW (2009) A thoracic mechanism of mild traumatic brain injury due to blast pressure waves. *Med Hypotheses* 72:76–83.
7. Lusardi TA, Rangan J, Sun D, Smith DH, Meaney DF (2004) A device to study the initiation and propagation of calcium transients in cultured neurons after mechanical stretch. *Ann Biomed Eng* 32:1546–1558.
8. Pfister BJ, Weihs TP, Betenbaugh M, Bao G (2003) An in vitro uniaxial stretch model for axonal injury. *Ann Biomed Eng* 31:589–598.
9. Alford PW, Taber LA (2003) Regional epicardial strain in the embryonic chick heart during the early looping stages. *J Biomech* 36:1135–1141.
10. Bray MA, Sheehy SP, Parker KK (2008) Sarcomere alignment is regulated by myocyte shape. *Cell Motil Cytoskeleton* 65:641–651.
11. Bray MA, et al. (2010) Nuclear morphology and deformation in engineered cardiac myocytes and tissues. *Biomaterials* 31:5143–5150.
12. Coppin CM, Leavis PC (1992) Quantitation of liquid-crystalline ordering in F-actin solutions. *Biophys J* 63:794–807.
13. Geddes DM, Cargill RS, 2nd, LaPlaca MC (2003) Mechanical stretch to neurons results in a strain rate and magnitude-dependent increase in plasma membrane permeability. *J Neurotrauma* 20:1039–1049.
14. Rodriguez EK, Hoger A, McCulloch AD (1994) Stress-dependent finite growth in soft elastic tissues. *J Biomech* 27:455–467.
15. Taber LA (1998) Biomechanical growth laws for muscle tissue. *Journal of Theoretical Biology* 193:201–213.
16. Taber LA (1998) A model for aortic growth based on fluid shear and fiber stresses. *J Biomech Eng-Trans ASME* 120:348–354.
17. Alford PW, Humphrey JD, Taber LA (2008) Growth and remodeling in a thick-walled artery model: effects of spatial variations in wall constituents. *Biomech Model Mechanobiol* 7:245–262.
18. Alford PW, Taber LA (2008) Computational study of growth and remodelling in the aortic arch. *Comput Methods Biomech Biomed Engin* 11:525–538.
19. Gleason RL, Humphrey JD (2004) A mixture model of arterial growth and remodeling in hypertension: altered muscle tone and tissue turnover. *J Vasc Res* 41:352–363.
20. Rachev A, Gleason RL, Jr. (2010) Theoretical study on the effects of pressure-induced remodeling on geometry and mechanical nonhomogeneity of conduit arteries. *Biomech Model Mechanobiol* 10:79–93.
21. Ramasubramanian A, et al. (2008) On modeling morphogenesis of the looping heart following mechanical perturbations. *J Biomech Eng-Trans ASME* 130:061018-1–061018-11.
22. Owens GK, Kumar MS, Wamhoff BR (2004) Molecular regulation of vascular smooth-muscle cell differentiation in development and disease. *Physiol Rev* 84:767–801.
23. Rensen SS, Doevendans PA, van Eys GJ (2007) Regulation and characteristics of vascular smooth-muscle cell phenotypic diversity. *Neth Heart J* 15:100–108.
24. Holzapfel GA, Ogden RW (2010) Constitutive modelling of arteries. *Proceedings of the Royal Society a-Mathematical Physical and Engineering Sciences* 466:1551–1596.
25. Schmid H, et al. (2010) Impact of transmural heterogeneities on arterial adaptation. *Biomechanics and Modeling in Mechanobiology* 9:295–315.
26. Humphrey JD, Rajagopal KR (2003) A constrained mixture model for arterial adaptations to a sustained step change in blood flow. *Biomech Model Mechanobiol* 2:109–126.
27. Tsamis A, Stergiopulos N, Rachev A (2009) A structure-based model of arterial remodeling in response to sustained hypertension. *J Biomech Eng-Trans ASME* 131:101004-1–101004-8.
28. Gleason RL, Humphrey JD (2004) A mixture model of arterial growth and remodeling in hypertension: altered muscle tone and tissue turnover. *Journal of Vascular Research* 41:352–363.
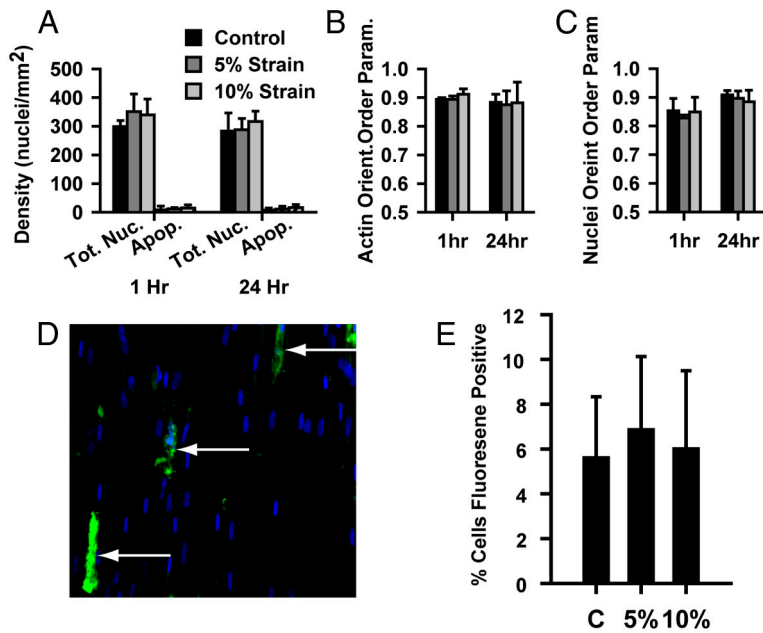
Fig. S1. Simulated blast does not significantly damage engineered vascular tissue (*A*) Tissue density is unchanged by simulated blast and apoptotic cells, as measured with a TUNEL assay, are an insignificant proportion of the population. (*B*) Actin alignment is unchanged by simulated blast. (*C*) Nuclear alignment is unchanged by simulated blast. (*D–E*) Membrane poration measured by fluoroscene dye uptake (*D*) Example image of fluorosene positive cells (indicated with arrows). (Scale bar, 200μm). (*E*) Simulated blast does not increase fraction of cells taking up dye, indicating that cells are not porating. Error bars: standard deviation.
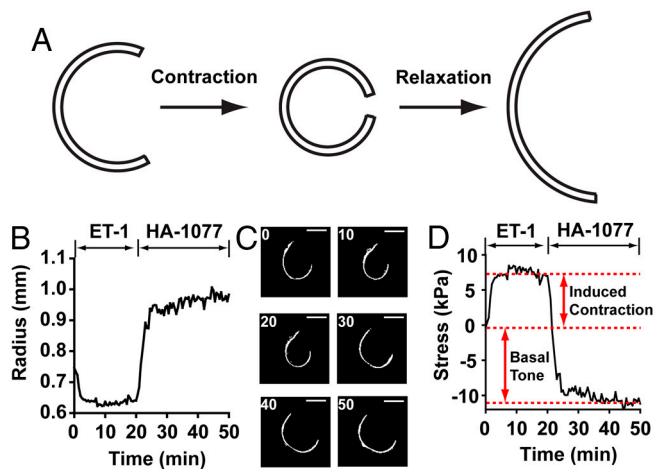
Fig. S2. Example vMTF temporal experimental data. (*A*) Contraction of vMTFs leads to a decreased radius of curvature, relaxation leads to an increased radius of curvature (*B*) vMTFs are serially stimulated with 50 nM ET-1 followed by 100 mM HA-1077, resulting in an initial decrease in radius of curvature followed by an increase in radius of curvature. (*C*) Example images of the vMTF at 0–50 min. (*D*) Calculated change in stress for the example vMTF. Induced contraction is measured as the difference in stress between the initial tissue stress and the stress after ET-1 treatment. Basal tone is the difference between the initial tissue stress and the stress after contraction is knocked out with HA-1077.
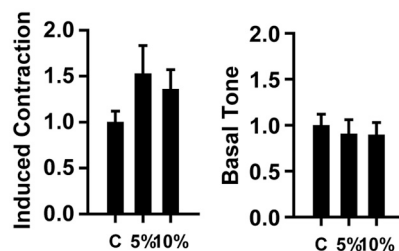

Fig. S3. ET-1 induced contraction and basal tone 1 h postblast in tissues treated with ROCK inhibitor immediately following blast.
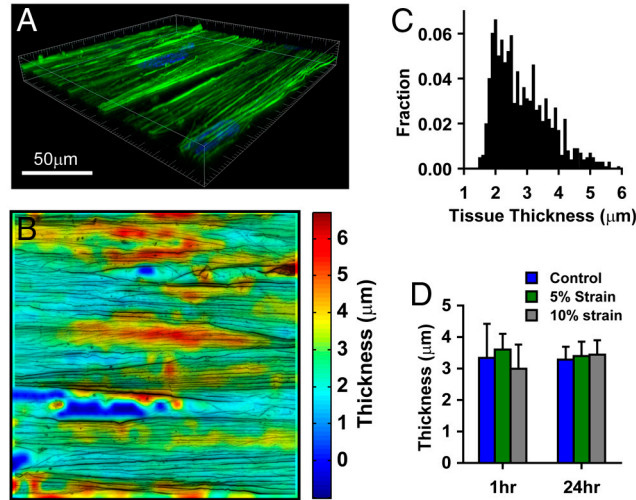
Fig. S4. Tissue thickness measurements. (*A*) Example confocal image of patterned VSMCs. (*B*) Example heat map of local thickness of the tissue (*C*) Tissue thickness distribution. (*D*) Mean tissue thicknesses for control and simulated blast tissues. There is no significant difference between treatment groups.
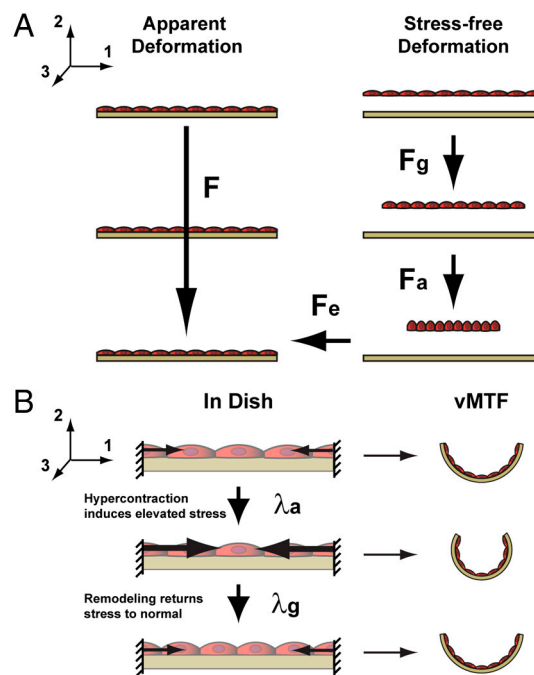

Fig. S5. Formulation for the mathematical model for blast-induced hypercontractility and stress-induces remodeling. (*A*) Schematic representation of the decoupled contraction and remodeling model. Apparent deformation is defined as **F**. Decoupled stress-free deformation of contraction is defined as **F$_a$**. Stress-free deformation due to growth and remodeling is **F$_g$**. Elastic deformation, used to calculate stress is **F$_e$**. (*B*) Schematic representation of hypercontraction induced growth. Blast injury induces hypercontarction defined as λ_a. This hypercontraction is measured experimentally by decreased radius of curvature of the vMTF. Adaptive remodeling λ_g returns the tissue stress, and vMTF curvature to equilibrium.
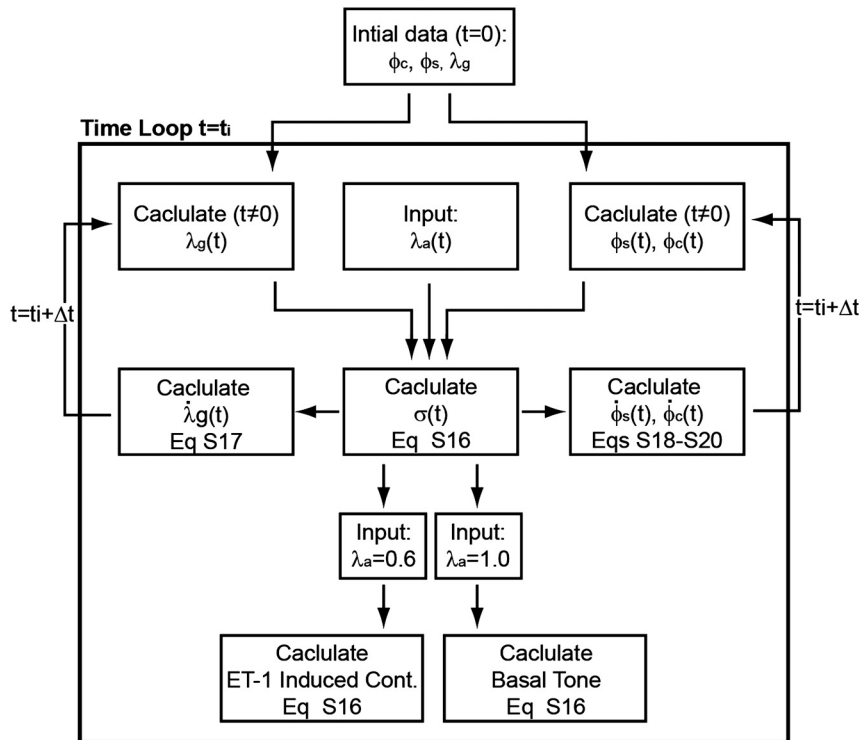
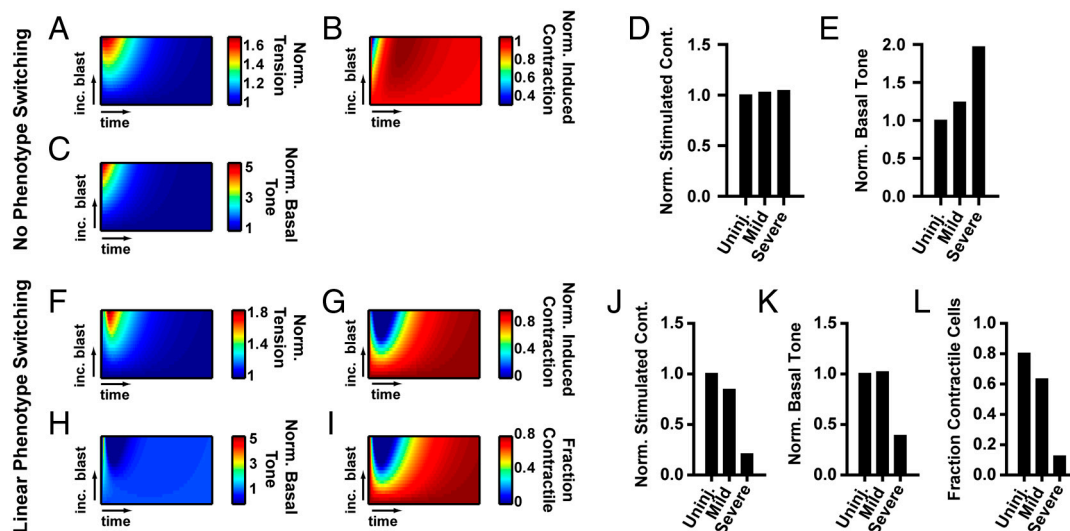**Fig. S6.** Flow chart for model calculations.

Fig. S7. Theoretical model for stress-induced remodeling with (*A–E*) no phenotype switching and (*F–L*) linear phenotype switching. (*A–C, F–I*) Contour plots of the temporal evolution of tissue tension, induced contraction, basal tone, and phenotype population for varying magnitudes of simulated blast. The *y*-axis represents tissues with increasing hypercontractility due to increasing blast injury (see *SI Text* for details). The *x*-axis represents the time after the blast. (*A, F*) Temporal stress evolution of remodeling tissue for varying blast-induced hypercontraction. (*B, G*) Model predicted induced contraction, (*C, H*) model predicted basal contractile tone for varying blast-induced hypercontraction. (*D*) Predicted temporal change in fraction of contractile cells for varying blast-induced hypercontraction and tissue remodeling. (*E–F, J–K*) Time point snapshots of (*E, J*) induced contraction, (*F, K*) basal tone, and (*G*) fraction contractile cells at an early time vasospasm development, indicated by the vertical line in (*A*), for mild injury, indicated by the lower horizontal line in (*A*), or a more severe injury, indicated by the upper horizontal line in (*A*).
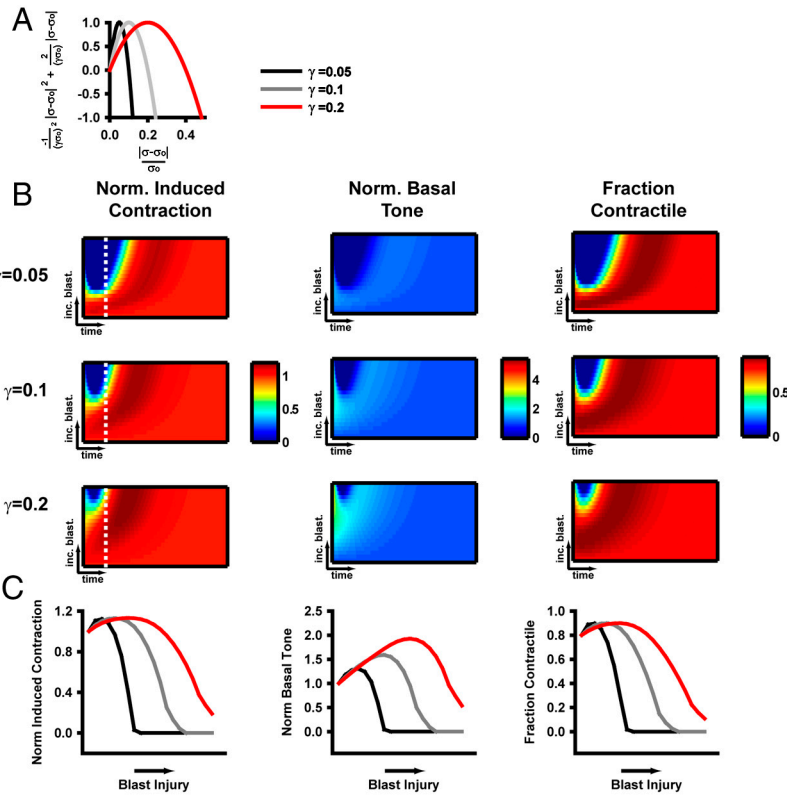
Fig. S8. Model parameter study. Value of γ, was varied to changing stress threshold criteria for transition from contractile to synthetic phenotype. (*A*) For three values of γ, stress-induced rate of change of phenotype (see Eq. **S21**) is shown as a function of perturbation from the target stress. (*B*) Heat maps representing the temporal change in induced contraction, basal tone, and fraction contractile cells for increasing blast injury for each value of γ. (*C*) Single time point (indicated by dotted line in *B*) plots showing model predicted nonlinear response to blast injury for induced contraction, basal tone and fraction contractile cells.
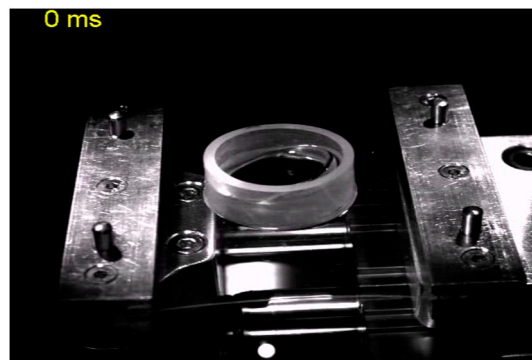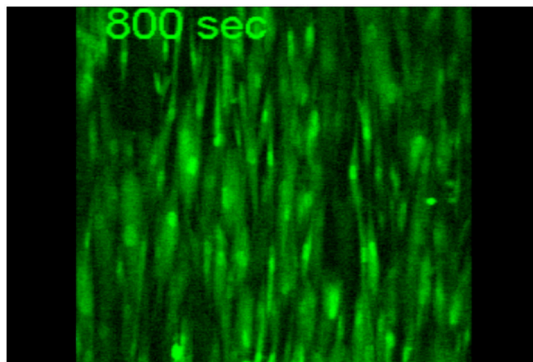

Movie S1. Simulated blast at 1,000 frames/sec. Stretchable substrate with tissue constructed on it is stretched 10% at strain rate 10,001/s.
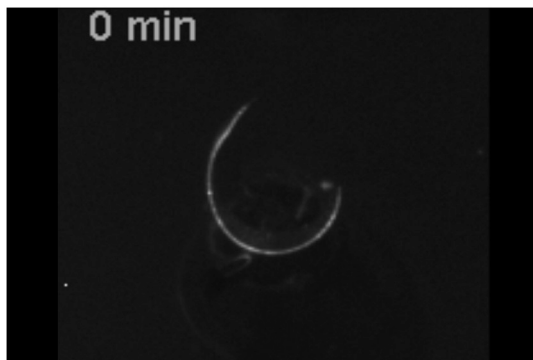
Movie SI (MPG)
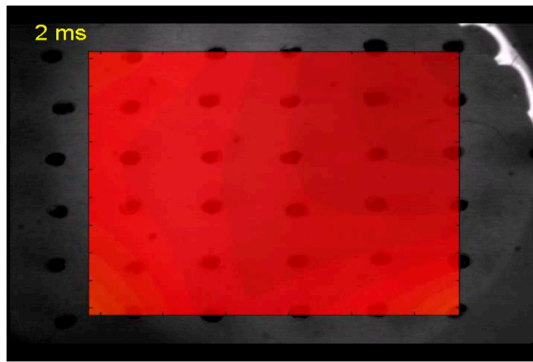
Movie S2. Surface deformation of stretchable substrate at 1,000 frames/sec used to calculate strain field of simulated blast

Movie S2 (MPG)

Movie S3. Representative movie of calcium dynamics during cytosolic calcium experiments.

Movie S3 (AVI)

Movie S4. Representative vMTF during serial stimulation with 50 nM ET-1 and 100 μM HA-1077, whose radius of curvature and stress is shown in Fig. S3.

Movie S4 (AVI)

Table S1. Parameters and constants used in the model

Parameters	Parameter description	Value
$\mathbf{F}$	deformation gradient tensor	
$\mathbf{F_e}$	elastic deformation tensor	
$\mathbf{F_a}$	active deformation tensor	
$\mathbf{F_g}$	redmodeling deformation tensor	
σ	Cauchy stress	
W	strain-energy density function	
p	Lagrange multiplier	
I_{e1}	first strain invariant	
λ_{ei}	elastic stretch ratio in the direction specified by i	
λ_{ei}	total stretch ratio in the direction specified by i	
λa	active stretch ratio	
λ_g	remodeling stretch ratio	
ϕ_c	fraction of cells with contractile phenotype	
ϕ_s	fraction of cells with synthetic phenotype	
α	degree of hypercontraciton	
Constants		Value
σ_o	target stress	20 kPa
C	material constant	3 kPa
τ_σ	remodeling related time constant	1,000 kPa/t
τ_a	contraction induced remodeling time constants	0.21/t
$\tau_{\phi\sigma}$	stress induced phenotype switching time constant	101/t
$\tau_{\phi\phi}$	phenotype induced phenotype switching time constant	11/t
γ	phenotype switch threshold constant	0.1
β	hyper-contraction time constant	0.1